

# Morphology-Directed Light Emission from Fluorescent Janus Colloids for Programmable Chemical-To-Optical Signal Transduction

Bradley D. Frank, Sara Nagelberg, Agata W. Baryzewska, Pablo Simón Marqués, Markus Antonietti, Mathias Kolle, and Lukas Zeininger\*

Materials capable of dynamically and reversibly altering their emission are relevant for numerous optical applications. Here, the anisotropic morphology-directed light emission from fluorescent Janus emulsion droplets, an intrinsically chemo-responsive material platform, is investigated. Informed by experimental observations of morphology-dependent optical confinement of internally emitted light within the higher refractive index phases, ray-tracing is used to predict and fine-tune the droplets' optical properties and their ability to concentrate light. Theoretical prediction and closely matching experimental results show that the collection of incident light and the confinement of emitted light in the internal droplet phase due to total internal reflection both contribute to the droplets' anisotropic light emission profile. A novel ratiometric dual-angle fluorescence detection approach that exploits the gravitational alignment of the droplets is implemented to quantify the morphology-dependent large-scale chemically-induced modulation of the anisotropic emission of droplet layers. Relevant emulsion design parameters are systematically examined to enhance the signal-to-noise ratio, and a second emitter is co-compartmentalized inside the droplets to amplify the anisotropic light confinement via an absorption–emission cascade. Preferential excitation of dyes in proximity to the internal droplet interface enhances the collected light intensity, demonstrating that dye-loaded Janus emulsion droplets function as stimuli-responsive, tunable, fluorescent optical elements.

## 1. Introduction

Transducing information via optical signals is a common strategy in information technology, signature management, and sensing.<sup>[1–6]</sup> The material foundation of these technologies are often nano- and microparticle-based emitters and scatterers,<sup>[7–9]</sup> that influence the magnitude and direction of emitted optical energy or alter the pathway of environmental light via electrical, magnetic, optical, or chemical activation.<sup>[10–14]</sup> Using light to store and transmit data is frequently a key approach in simple, low-cost, and high-speed strategies for processing information that can easily be multiplexed.<sup>[15–19]</sup> New stimuli-responsive colloidal materials that are capable of reversibly modulating their light-attenuating,<sup>[20,21]</sup> light-collecting,<sup>[22–24]</sup> or fluorescent<sup>[25–27]</sup> behavior and in addition can undergo a trigger-induced switch between different optical states (e.g., translucent or opaque), hold promise to improve and expand the capabilities of current technologies.<sup>[28,29]</sup>

In this context, bi-phasic Janus emulsions have recently emerged as useful optical elements.<sup>[30]</sup> Their unique refractory


optical properties are enabled by the gravitational alignment of the individual droplet phases, the adjustable refractive index contrast of the dispersed phase fluids, and tunable emulsion morphologies.<sup>[31]</sup> As a consequence, Janus droplets can manipulate the pathway of transmitted light and further present intriguing refractive, reflective, and emissive properties.<sup>[5,14,31,32]</sup> These properties provide the basis for a diverse range of optical applications of Janus emulsions, including as liquid compound microlenses,<sup>[31]</sup> for the generation of iridescent structural colors,<sup>[14,33]</sup> modular sensory layers on waveguides and optical resonator devices,<sup>[21,34]</sup> and as droplet-based solar concentrators.<sup>[23]</sup>

The balance of interfacial tensions acting between the droplet phases and the surrounding continuous medium dictates the internal geometry of Janus droplets comprised of two phase-separated fluid components.<sup>[35]</sup> As a result, the droplet morphology is reversibly configurable after droplet generation via chemical or physical manipulation of the interfacial

B. D. Frank, A. W. Baryzewska, P. Simón Marqués, M. Antonietti, L. Zeininger

Department of Colloid Chemistry  
Max Planck Institute of Colloids and Interfaces  
Am Muehlenberg 1, 14476 Potsdam, Germany  
E-mail: lukas.zeininger@mpikg.mpg.de

S. Nagelberg, M. Kolle  
Department of Mechanical Engineering  
Massachusetts Institute of Technology  
77 Massachusetts Avenue, Cambridge, MA 02139, USA

 The ORCID identification number(s) for the author(s) of this article can be found under <https://doi.org/10.1002/adom.202300875>

© 2023 The Authors. Advanced Optical Materials published by Wiley-VCH GmbH. This is an open access article under the terms of the Creative Commons Attribution-NonCommercial-NoDerivs License, which permits use and distribution in any medium, provided the original work is properly cited, the use is non-commercial and no modifications or adaptations are made.

DOI: 10.1002/adom.202300875

tension equilibrium.<sup>[36]</sup> By exploiting this unique chemical–morphological coupling, selective programming of individual droplet interfaces with stimuli-responsive surfactants has enabled a variety of Janus emulsion-based technologies, including batch techniques to generate precise anisotropic objects,<sup>[37–39]</sup> and modular liquid sensing platforms targeting small molecules,<sup>[40,41]</sup> metal ions,<sup>[42–44]</sup> viruses,<sup>[27,28]</sup> or bacteria.<sup>[5,45,46]</sup> Central to these sensing platforms is a reliable modulation of the optical properties of Janus droplets in response to chemical stimulation that generates an easily readable output signal. In this context, fluorescent Janus droplets are promising modular probes that can convey signals unencumbered from the chemical interactions at the droplet interface that modify the internal droplet morphology.<sup>[5,40,41,47]</sup> To facilitate broad implementation of Janus emulsion-based fluorescent probes in sensing platforms, a complete understanding of the emulsions' unique chemical–morphological–optical coupling is required in order to optimize the signal-to-noise ratio, and allow for quantitative signal transduction and amplification. Specifically, deployment of Janus emulsions as on-site sensors requires a simple characteristic readout method which is self-referential, and applicable to polydisperse, simple-to-prepare samples. Control over their ability to selectively display and attenuate fluorescent signals moreover promises to expand the scope of Janus droplet optical elements to a range of other transformative applications, including data transmission, signature management, and display technologies.

Here, we report a detailed study aimed at understanding and optimizing the anisotropic light-emission characteristics of fluorescent Janus emulsions that combines predictive ray-tracing calculations with experimental observations. We started by recording the angle-dependent emission intensity of different bi-phasic droplet morphologies using a customized emission angle-sensitive fluorescence microscope. To fully understand the emulsions' observed optical behavior, we then implemented a two-step ray-tracing model in which we investigated the anisotropic light-emission characteristics of Janus emulsions containing a fluorescent dye compartmentalized within one of the droplet phases, accounting for both the concentration of incident light and confinement of internally emitted light. Based on our theoretical and experimental findings, we establish a predictive model, which closely captures the measured anisotropic light-emission characteristics of Janus droplets that act as luminescence concentrators. We complement the analysis of the emulsions' light-emission properties with the development of a simple macroscale read-out method that does not require specialized microscopic techniques and instead relies on ratiometric, dual-angle quantification of the emission intensity of gravitationally aligned polydisperse Janus droplet layers, which can be easily produced in nearly any environment. We use our predictive model to assess how the droplet's anisotropic emission can be tailored by adjusting the refractive index contrast and volume ratio of the droplet phases. Finally, we also investigated how selective co-solubilization of multiple fluorescent dyes presenting an energetic overlap of the absorption and emission band can enhance the signal-to-noise ratio. In summation, our comprehensive assessment and optimization of droplet emission characteristics, paired with defining an optical read-out strategy, allows us to present a method for reference-free, ratiometric detection and

sensing of chemically evoked changes in complex droplet morphologies solely from their emission profile that can be easily implemented.

## 2. Results and Discussion

### 2.1. Imaging of the Anisotropic Droplet Luminescence

To observe the angle-dependent fluorescence intensity of dye-loaded Janus emulsion droplets and to assess the emulsion's potential to function as droplet luminescence concentrators (DLCs), we prepared emulsion droplets comprised of a mixture of hydrocarbon (HC) and fluorocarbon (FC) oils with a large density contrast and a pronounced refractive index difference, namely, diethylbenzene (DEB,  $\rho_{\text{HC}} = 0.87 \text{ g mL}^{-1}$ ,  $n_{\text{HC}} = 1.495$ ) and HFE-7500 (HFE,  $\rho_{\text{FC}} = 1.61 \text{ g mL}^{-1}$ ,  $n_{\text{FC}} = 1.287$ ). A large density contrast of the two droplet phases ensures gravitational alignment, enabling a uniform orientation of individual droplets assembled across large areas to form macroscopic droplet-based optical systems and sensors. Phase-selective molecular partitioning enables the homogenous distribution of fluorescent dyes, such as perylene ( $1 \times 10^{-3} \text{ M}$ ), within the high refractive index DEB hydrocarbon phase. The large refractive index contrast of DEB and HFE enables total internal reflection (TIR) along the internal interface of bi-phasic emulsion droplets. Janus droplets made from DEB and HFE assume an overall close-to-spherical shape due to the negligibly small interfacial tension ( $\approx 0.5 \text{ mN m}^{-1}$ ) between the two dispersed oil phases compared to the hydrocarbon–water and fluorocarbon–water interfacial tensions ( $\approx 5 \text{ mN m}^{-1}$ ).<sup>[35]</sup> Variation of the balance of interfacial tensions, e.g., achieved by changing the ratio of hydrocarbon (sodium dodecyl sulfate; hereafter SDS) and fluorocarbon (Zonyl FS-300; hereafter Zonyl) surfactants within the continuous phase transduces into dynamic changes in internal droplet morphology. The contact angle at the three-phase junction between DEB, HFE, and the aqueous medium quantitatively describes specific Janus droplet morphologies (Figure 1a).<sup>[31]</sup>

To visualize the Janus droplets' angle-dependent anisotropic emission intensity (Figure 1b), we utilized a customized rotating fluorescence microscope that enabled direct imaging of the collected light of gravitationally aligned droplets from any angle in the range of  $0^\circ$ – $90^\circ$  (Figure 1c). We placed perylene-containing ( $c = 1 \times 10^{-3} \text{ M}$  in the DEB phase) Janus droplets into a sample holder and captured fluorescence micrographs while rotating the microscope. When applying UV light ( $\lambda = 385 \text{ nm}$ ) to the droplets, a spatially concentrated angle-dependent signature of perylene fluorescence was observed in the proximity of the three-phase contact line. This emission signature could be dynamically enhanced or attenuated as a function of the specific Janus droplet morphology and the observation angle.

More specifically, when observing the droplet fluorescence vertically (microscope angle of  $0^\circ$ ), Janus emulsions with an “opened-up” fluorocarbon-dominant morphology (three-phase contact angle of  $\theta_{\text{CA}} \approx 26^\circ$ ) displayed an annular signature of significantly enhanced fluorescence adjacent to the three-phase contact line (Figure 1b). Further expansion of the hydrocarbon–water interface toward contact angles of  $\theta_{\text{CA}} \approx 60^\circ$  resulted in a reduction of vertically directed fluorescence intensity (Figure 1d). However, a strong emission intensity signal could then be observed

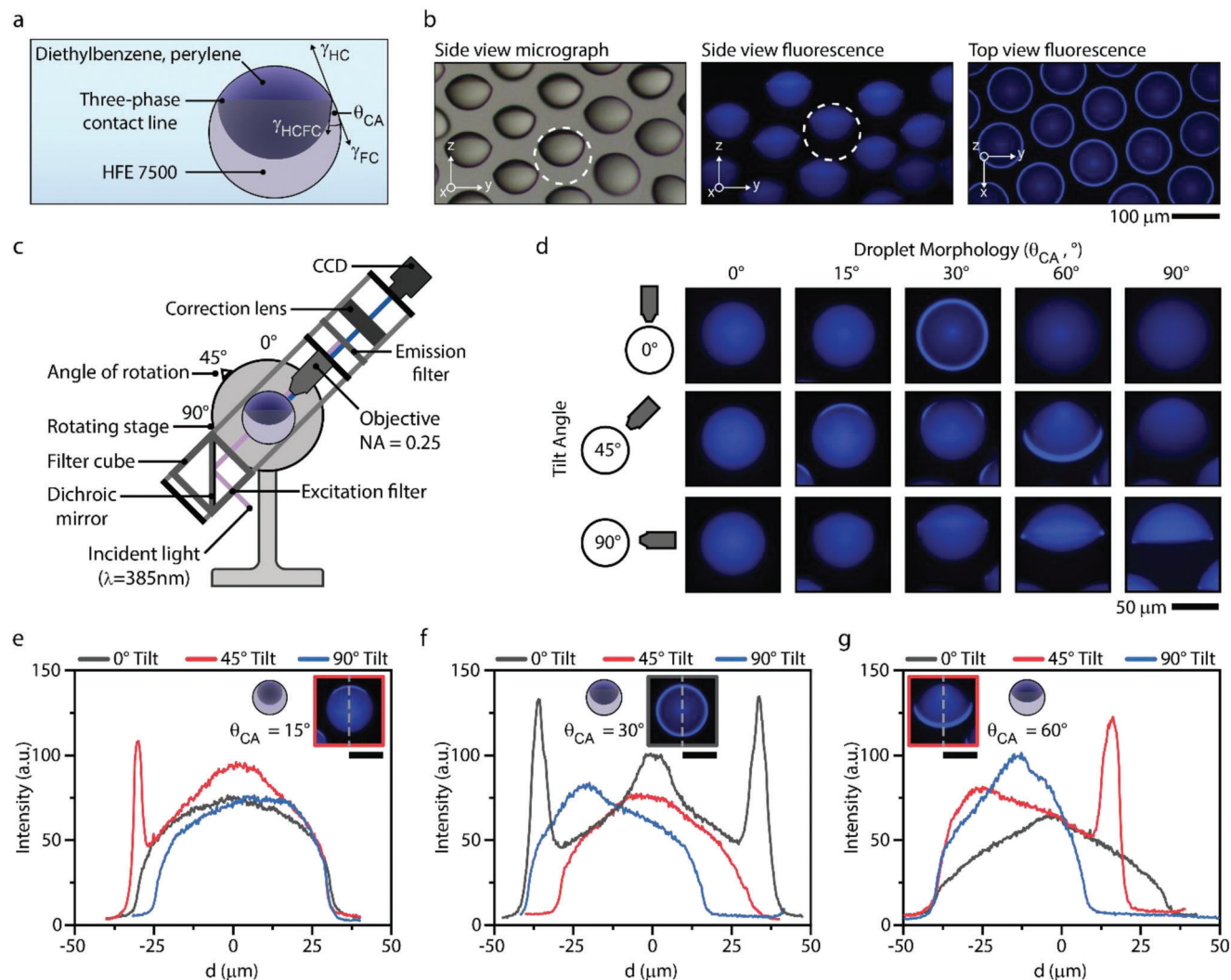


**Figure 1.** Morphology-dependent anisotropic light emission from fluorescent Janus emulsions. a) Schematic of droplet composition and morphology that is defined by the balance of interfacial tensions, and quantitatively described by the contact angle  $\theta_{CA}$ . b) Bright-field optical and fluorescence side-view and top-view micrographs displaying fluorescent Janus droplets with a contact angle of  $\theta_{CA} = 26^\circ$ . c) Schematic illustration of the customized rotating fluorescence microscope composed of a rotating stage, infinity correction lens, objective, filter cube (excitation filter:  $390 \pm 9$  nm, dichroic mirror  $360\text{--}407$  nm reflection, and  $425\text{--}475$  nm transmission), emission filter ( $460 \pm 30$  nm), and sample holder, used to image the light emission of gravitationally aligned perylene-containing Janus droplets from different angles. d) Fluorescence micrographs of DEB:HFE droplets in five morphologies containing perylene compartmentalized in the upper hydrocarbon phase from three different viewing angles ( $0^\circ$ ,  $45^\circ$ ,  $90^\circ$ ). e–g) Vertical line profile intensity for a perylene-containing DEB:HFE7500 droplet with a contact angle of  $\theta_{CA} = 15^\circ$  for (e),  $\theta_{CA} = 30^\circ$  for (f), and  $\theta_{CA} = 60^\circ$  for (g), observed at angles of  $0^\circ$  (gray),  $45^\circ$  (red), and  $90^\circ$  (blue) with inset fluorescence micrographs for the noted observation angle by color outline (scale bar =  $50 \mu\text{m}$ ).

upon tilting the microscope to  $45^\circ$ . Similarly, droplets displayed increased light intensities in the  $45^\circ$ -direction when adjusting the droplet morphology to contact angles of  $\theta_{CA} \approx 15^\circ$ , thereby “closing up” the droplet morphology. The observations indicate that reconfigurable emissive emulsion droplets can redistribute and concentrate emitted light at various angles and locations around the droplet as a function of the shape of the internal droplet interface.

Nonnormalized fluorescence intensity line profiles (obtained from vertical sections through the center of droplet images) display the morphology-dependent enhancement of light intensity adjacent to the internal interface (Figure 1e–g), which results from total internal reflection of light at the hydrocarbon–

fluorocarbon interface.<sup>[5]</sup> From these intensity profiles, we extract the ratio of the intensity maximum emitted near the three-phase junction and the intensity emitted at the droplet apex (center of droplet image). This ratio  $S = I_{\text{peak}}/I_{\text{center}}$  is pronounced for droplets with a three-phase contact angle of  $\theta_{CA} \approx 30^\circ$  observed from the vertical direction ( $S = 1.34$ , black trace in Figure 1f), while there is no detectable intensity peak observed in the other observation directions. A large ratio of  $S = 1.74$  can also be measured for droplets with a three-phase contact angle  $\theta_{CA} \approx 60^\circ$  observed at an angle of  $45^\circ$  (Figure 1g, red trace), while  $S$  is small for the other two observation angles. Fully encapsulated double emulsion droplets ( $\theta_{CA} \approx 0^\circ$ ) result in  $S \approx 1$  from either of the three viewing directions. Thus, whereas bi-phasic droplets in an

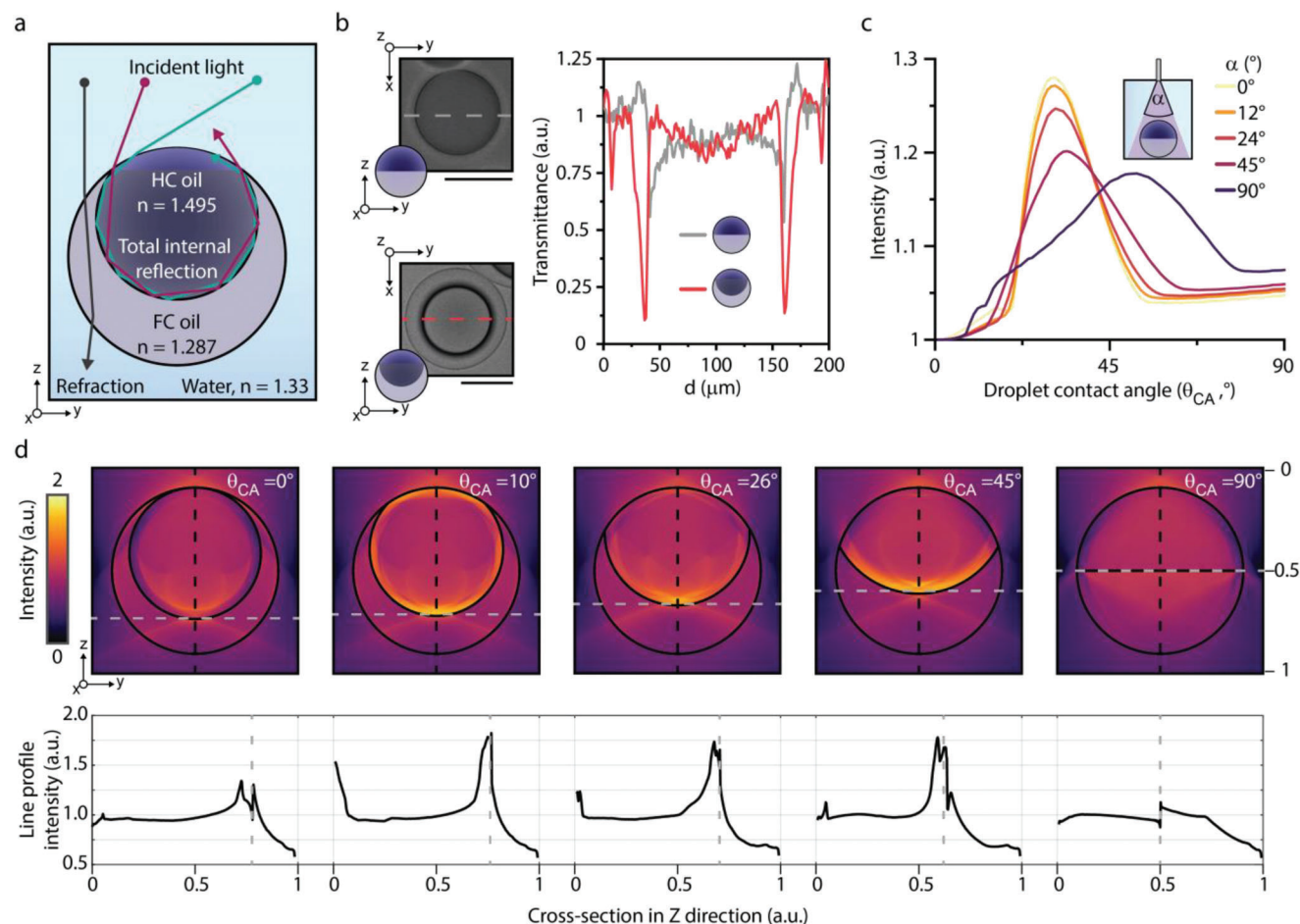


**Figure 2.** Janus droplet morphology affects incident light field in droplets. a) Schematic depiction of the interaction of incident light with an emulsion droplet. b) Side-view schematics for droplets and vertical transmission light top-view micrographs of droplets that collect and transmit incident light, with inset line profiles of transmitted light intensity; scale bar: 50  $\mu\text{m}$ . c) Modeled collected light intensity of incident light inside the hydrocarbon phase for Janus droplets in different morphologies; with different angular distributions ( $\alpha$ ) of the incident light rays, where  $0^\circ$  corresponds to a collimated light source, and  $90^\circ$  corresponds to incident rays distributed in a  $90^\circ$  cone. d) Simulated 2D intensity maps of Janus emulsion droplets for broad incident light collection based on morphology with corresponding vertical line profile of intensity.

encapsulated double emulsion morphology ( $\theta_{CA} = 0^\circ$ ) revealed no measurable variation in angular emitted light intensity, Janus droplets displayed a strongly angle- and morphology-dependent perylene emission.

## 2.2. Modeling Incident Excitation Light Distribution

The emulsion droplets change the incident light field via refraction and total internal reflection (Figure 2a). Depending primarily on droplet composition, morphology, and angle of incident light illumination, the effect of refraction and total internal reflection may cause an anisotropic distribution of the incoming excitation light throughout the perylene-loaded hydrocarbon phase. We hypothesized that an anisotropic distribution of excitation light intensity would contribute to and affect the Janus droplets' emission characteristics. Therefore, we started by modeling the incident light concentration inside fluorescent emulsion droplets. Such considerations were corroborated by experimental obser-

vations, where significant differences in the light transmission between Janus droplets in slightly "opened-up" ( $\theta_{CA} = 30^\circ$ ) and perfect Janus ( $\theta_{CA} = 90^\circ$ ) geometries were observed in the respective optical micrographs (Figure 2b). We placed droplets of these two morphologies in an optical microscope in transmission mode and measured line profiles of the transmitted light intensity across the droplets. Whereas for a perfect Janus emulsion droplet, minimal TIR of light at the internal droplet interface was observed (Figure 2b, top left), transmission optical micrographs of Janus droplets in a morphology of  $\theta_{CA} = 26^\circ$  displayed a characteristic dark ring in proximity to the three-phase contact line (Figure 2b, bottom left). This can be attributed to refraction and light diverted away from the optical axis of the microscope. A light intensity cross-section of the two droplets displays the significant differences in excitation light passing through the droplets toward the observing microscope objective (Figure 2b, right).

To understand and quantify the distribution of excitation light throughout the droplet, we modeled the propagation of incoming light using a customized ray-tracing algorithm in MATLAB.

In this algorithm, incident light rays ( $N = 10^7$ ) are propagated from above to a droplet with radius  $R$  at a distance of  $d = 3R$ . In our calculations, Snell's law and the Fresnel equations dictate the refraction and reflection amplitudes of light rays interacting with the droplets. To approximate physically realizable light exposures of droplet samples, rays are given randomized starting directions and positions defined by the emission profile of the light sources used in our experiments, which were either an optical fiber with a numerical aperture  $NA = 0.22$  and an emission cone of  $24^\circ$  or a collimated light source with an emission angle of  $0^\circ$ . In our 2D ray-tracing model, the droplets were considered large with respect to the wavelength of the incident light, and ray trajectories were traced throughout the Janus droplets based on the characteristic refractive index contrast of the constituent phases and the three morphology-dependent interfaces. All paths and amplitudes of rays were saved as they were traced through the droplet, and intensity maps were generated using a bicubic projection of ray paths and amplitudes to quantify the light intensity. Thus, light distribution within the droplets could be defined as the intensity for a given pixel after the ray-tracing experiment.

The magnitude of total internal reflection of incident light significantly depends on droplet geometry. In addition, the amount of total internal reflection is also dependent on the angular distribution of incident light. Only incident light rays which interact with the hydrocarbon–fluorocarbon interface at an angle below the critical angle will totally internally reflect. Our ray-tracing model confirmed this dependence of light distribution inside the droplets on the angle of the incident light and the droplet geometry (Figure 2c). When modeling a collimated light source, we determined pronounced differences in the observed light intensity for droplets of different morphologies partly due to the total internal reflection of incoming light at the curved internal interface between the hydrocarbon and the fluorocarbon (Figure 2c). The intensity of incident light is estimated as the sum of simulated ray intensity maps within the hydrocarbon phase. To understand the influence of incident light direction, we vary the total distribution angles of incident light to the droplet, where collimated light corresponds to a distribution angle of  $0^\circ$  (Figure 2c). Consequently, opened-up Janus droplets in a morphology defined by the three-phase contact angle of  $\theta_{CA} = 26^\circ$  displayed a characteristic concentration of incoming light intensity in proximity to the droplet internal high refractive–low refractive index interface (Figure 2d). In turn, for droplets approaching an encapsulated ( $\theta_{CA} \rightarrow 0^\circ$ ) or perfect Janus morphology ( $\theta_{CA} \rightarrow 90^\circ$ ), only a marginal concentration of incoming light at the internal interface was determined (Figure 2d). Upon broadening the angles of incident light delivery to  $45^\circ$  or  $90^\circ$ , mimicking a more diffuse light source, we observed a broadening of the contact angle range at which light could be concentrated via TIR at the internal interface, and the light intensity profile was consequently enhanced. For light delivered in a cone with an apex angle of  $90^\circ$  from above the droplets, the amount of collected light decreased, and a broader range of droplets was enabled to concentrate light along the internal droplet interface, from  $\theta_{CA} = 20^\circ$ – $45^\circ$  for  $12^\circ$  light to  $\theta_{CA} = 20^\circ$ – $74^\circ$  for  $90^\circ$  light. Profiles of intensity perpendicular to the droplet internal interface reveal the influence of the droplet morphology on the light concentration at the internal interface (Figure 2d). Droplets with a sizeable refractive index contrast and a sufficiently small internal radius of curvature, enabling total in-

ternal reflection, could trap light via TIR along the hydrocarbon–water interface and the hydrocarbon–fluorocarbon interface ( $\theta_{CA} = 10^\circ$ , Figure 2d). All other droplet morphologies which collected TIR light and guided it along the internal interface present similar peak intensities of concentrated light along the hydrocarbon–fluorocarbon interface ( $\theta_{CA} = 26^\circ$ ,  $\theta_{CA} = 45^\circ$ , Figure 2d). The observed concentration of the light field has implications for the droplets' angle-dependent luminescence since regions of higher excitation light intensity, at constant fluorophore quantum yield, translate into higher emission intensities.

### 2.3. Modeling Emission Trajectories

Similar to the trajectories of incident light within the droplet, light that is emitted from inside the higher refractive index droplet phase can undergo total internal reflection at the internal droplet interface. Depending on the droplet's morphology and the starting location and direction of emitter rays, fluorescent light is emitted from the droplet after refraction at one or more droplet interfaces or interacts with the internal droplet interface at an angle larger than the critical angle of TIR  $\theta_c = 64.8^\circ$ , in which case total internal reflection guides rays along the concave internal droplet interface. When collected total internally reflected light rays encounter the external hydrocarbon–water interface, they can escape the droplet near the three-phase contact line at a morphology-dependent angle (Figure 3a).

In a simple geometrical model, we can estimate the direction and range of possible angles of totally internally reflected light rays exiting the droplets (for details see the Supporting Information). In this model, we find two edge cases (Figure 3a) which define the boundaries of TIR light emission from droplets in different morphologies. The angular range of light that is guided along an interface is limited by the critical angle of total internal reflection of that interface  $\theta_c$ . The first limiting case is given by light rays that intersect with the hydrocarbon–water interface after a reflection at the internal interface, where they undergo refraction at the external droplet interface according to Snell's law (Figure 3a, Case a). It should be noted that for small droplet contact angles, the collected TIR rays can also reflect at the hydrocarbon–water interface above the critical angle of TIR of that interface and are therefore reflected and do not exit the droplet near the three-phase contact line, which limits the range of angular emission (Figure 3a, case a). The second case describes the angular limit of totally internally reflected light rays that are refracted at the hydrocarbon–water interface just before reflection at the hydrocarbon–fluorocarbon interface near the three-phase contact line (Figure 3a, case b). The total angular range of enhanced emission near the three-phase contact line is then specified by the two limiting angles for the edge cases  $\theta_a$  and  $\theta_b$ , which define the morphology-dependent direction of emitted light collected along the internal interface in proximity to the three-phase contact line relative to the droplets' gravitational axis.

Comparing these considerations to the fluorescence micrographs of dyed Janus emulsions at different angles reveals that this simple geometrical model could be used to predict the angular range of enhanced light intensities around emissive droplets (Figure 3b), whereas it does not quantitatively capture any differences in the emitted angular light intensity profiles. To model

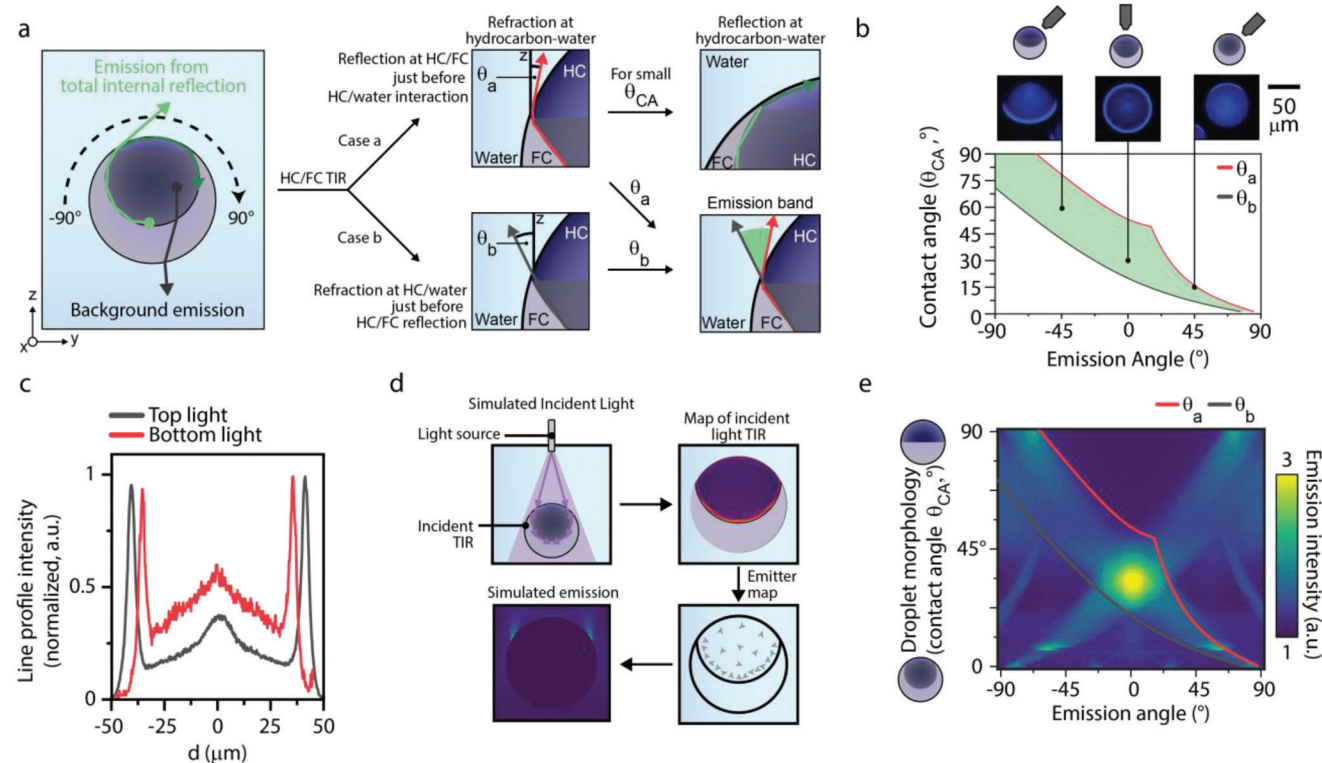


**Figure 3.** Light emission from droplet luminescence concentrators. a) Schematic depicting different trajectories of light exiting a complex emulsion droplet as either background emission or emission from total internally reflected light responsible for the anisotropic emission intensity profile, with a geometrical edge-case model to estimate the angular range of the emission band. b) Graph displaying the possible angular range of the emission band near the three-phase contact line with respect to the droplet gravitational axis for Janus droplets in different morphologies, with inset fluorescence micrographs of dyed complex emulsion droplets imaged from different angles. c) Line profile intensity (normalized from 0 to 1) of fluorescence micrographs for droplets (DEB:HFE) with a contact angle of  $\approx 30^\circ$  with perylene in the hydrocarbon phase, with UV light delivered either from the top or bottom of the droplet. d) Scheme for the two-step ray tracing model of droplet emission from the incident light collection. e) 2D normalized intensity map of droplet morphology versus emission angle including an indication of the angular limits of enhanced light emission from the geometrical model in (b).

the emitted light intensity profiles, we tracked the propagation of emitted light from inside the hydrocarbon phase using the customized ray-tracing algorithm. In our calculations, we account for the concentration of incident light inside the hydrocarbon phase prior to the dye excitation by simulating variable light concentrations throughout the hydrocarbon phase depending on the droplet morphology.

To place the influence of incident light concentration on the emission intensity profiles in an experimental context, we experimentally compared the emission profiles of emissive droplets excited with light delivered from above or below the droplet layers. In both cases, droplets display an annular ring of fluorescence close to the three-phase contact line. However, when light was delivered from above the droplet layers, thus enabling total internal reflection of incident light, the annular fluorescence contrast was higher. We normalized the line intensity profiles for each case to understand the contribution of incident light total internal reflection for enhancing fluorescence at the three-phase contact line (signal) in comparison to background fluorescence in the droplet center (noise). The emission profiles of droplets that emit light vertically displayed strong differences in the signal-to-noise ratio ( $S = I_{\text{peak}}/I_{\text{center}}$ ) of  $S = 2.63$  for light delivered from

above, which compares to  $S = 1.59$  for light delivered from below the droplets, respectively (Figure 3d).

To simulate the variable intensity distribution of incident light throughout the fluorescent droplet phase, we initialize emitter rays ( $N > 10^7$ ) with randomized starting directions and a spatial density distribution that matches the intensity distribution of incident excitation light, as higher levels of emission should be expected where higher levels of excitation intensities are present (Figure 3e). Thus, the Janus droplets' radial emission signature is modeled in two steps: first, incident light intensity maps are used to generate a density distribution of emitters with randomized emission direction within the hydrocarbon phase. Then the trajectories of the rays originating from the emitters are traced to determine emitted light intensity distributions inside the droplets and to assess the direction and intensity of light emanating from the droplets.

The model assumes an excess of incident excitation light, neglecting probabilistic considerations of dye absorption as a function of variations in incident light levels within the droplet. The final amplitudes and locations of rays emitted from the droplets are then used to quantify the morphology-dependent anisotropic emission from fluorescent emulsion droplets (Figure 3e).

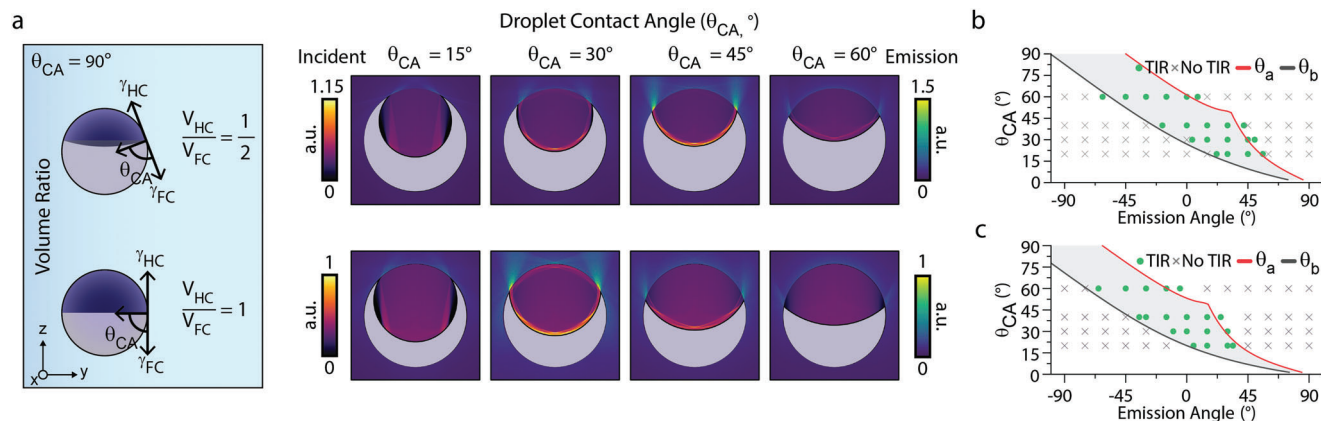


**Figure 4.** Droplet phase volume ratio affects the collection and concentration of light. a) Scheme for the effect of volume ratio on droplets with uniform contact angles ( $\theta_{CA} = 90^\circ$ ), and overlaid simulated incident light intensity and emission profile intensity maps for droplets composed of DEB and HFE7500 in water, with light delivered from a fiber probe (NA: 0.22); the two color bars separately display light intensities inside and outside the droplets, normalized to the maximum intensity within each set for one volume ratio. b) The calculated emission band as determined from geometrical modeling for droplets with a volume ratio of 0.5, with phase diagram of droplets which exhibit or do not exhibit total internal reflection at a given recording angle. c) Graph displaying the calculated emission band as determined from geometrical modeling for droplets with a volume ratio of 1, with phase diagram of droplets which exhibits or does not exhibit total internal reflection at a given recording angle.

Exposure and expansion of the hydrocarbon–water interface (increasing the three-phase contact angle) resulted in a pronounced increase in emission intensity. We observed the most pronounced angle-dependent emission output for droplets with a contact angle of  $\theta_{CA} = 26^\circ\text{--}32^\circ$ , which displayed enhanced incident light concentration near the internal interface and consequently increased emitted light intensity near that interface. A large proportion of the light emitted in the vicinity of the interface then propagates by total internal reflection along the interface and is coupled out near the three-phase contact line resulting in the observed spatially localized and angularly restricted emission peaks (Figure 1c–f). Droplets with contact angles larger than  $\theta_{CA} = 32^\circ$  presented peak emission intensities in the off-axis direction. Consequently, Janus droplets with a contact angle of  $\theta_{CA} \sim 60^\circ$  present an emission peak at a  $45^\circ$  viewing angle, which was in close agreement with the experimentally assessed DLC angular emission profiles, and consistent with the purely geometrical model. Simulated intensity out of the geometrical model is attributed to background intensity by nontotally internally reflect rays, and total internal reflection along the hydrocarbon–water interface.

With the model verified based on the close match between predictions and measurements (Figure 3b), we set out to further control the morphology-dependent emission signature from fluorescent bi-phasic emulsions. A critical design parameter influencing droplet morphology is the volume ratio of the two droplet constituent phases ( $V_{HC}/V_{FC}$ ). For the preceding discussion, all droplet morphologies were characterized by a volume ratio of  $V_{HC}/V_{FC} = 1$ . Deviations from an equal volume ratio cause predictable variations of the droplet emission intensity profile. In otherwise identical conditions, droplets of different volume ratios are characterized by the same contact angle ( $\theta_{CA}$ ),<sup>[42]</sup> as the volume ratio does not affect the interfacial tension equilibrium. Considering the concentration or emission of light, a nonuniform volume ratio results in a pronounced variation in the curvature of the internal interface and the location of the three-phase

contact line (Figure 4a). As described above, the location of the three-phase contact line is critical for the determination of the distribution and intensity profile of both excitation and emitted light.

We simulated droplets with a volume ratio of 0.5, 1, and 2 (Supporting Information Figure S6) to elucidate the opportunity in further tuning the morphology for a given droplet contact angle (Figure 4a). The calculations reveal that when varying the volume ratio, droplets of uniform contact angle display a different angular distribution of emitted light from total internal reflection. Changes in the location of the three-phase contact line alter the location of the vertical peak emission (Figure 4a), as predicted by the center of the emission band predicted from the geometrical model (Figure 4b,c), and measured as phase diagrams of droplets which exhibit or do not exhibit TIR at a particular recording angle (Figure 4b,c). Changes in the relative size of the hydrocarbon phase affect the radius of curvature of the internal droplet interface, thus influencing the relative amount of collected incident and emitted light that is totally internally reflected along the hydrocarbon–fluorocarbon interface (Supporting Information Figure S6). The dependence of angular emission profile on the droplet volume ratio outlines the opportunity to tune the direction of enhanced angular emission intensity independent of the interfacial tension equilibrium.

#### 2.4. Ratiometric Read-Out of Complex Droplet Morphologies

Motivated by our understanding of the angle-dependent droplet emission, we next set out to implement a simple-to-use ratiometric read-out platform that enables precise determination of droplet configuration based on their characteristic anisotropic emission signature. A ratiometric measurement of macroscale optical variation from emulsion droplet monolayers could utilize polydisperse complex emulsion samples, enabling the application as sensors with simple on-site batch droplet generation. We

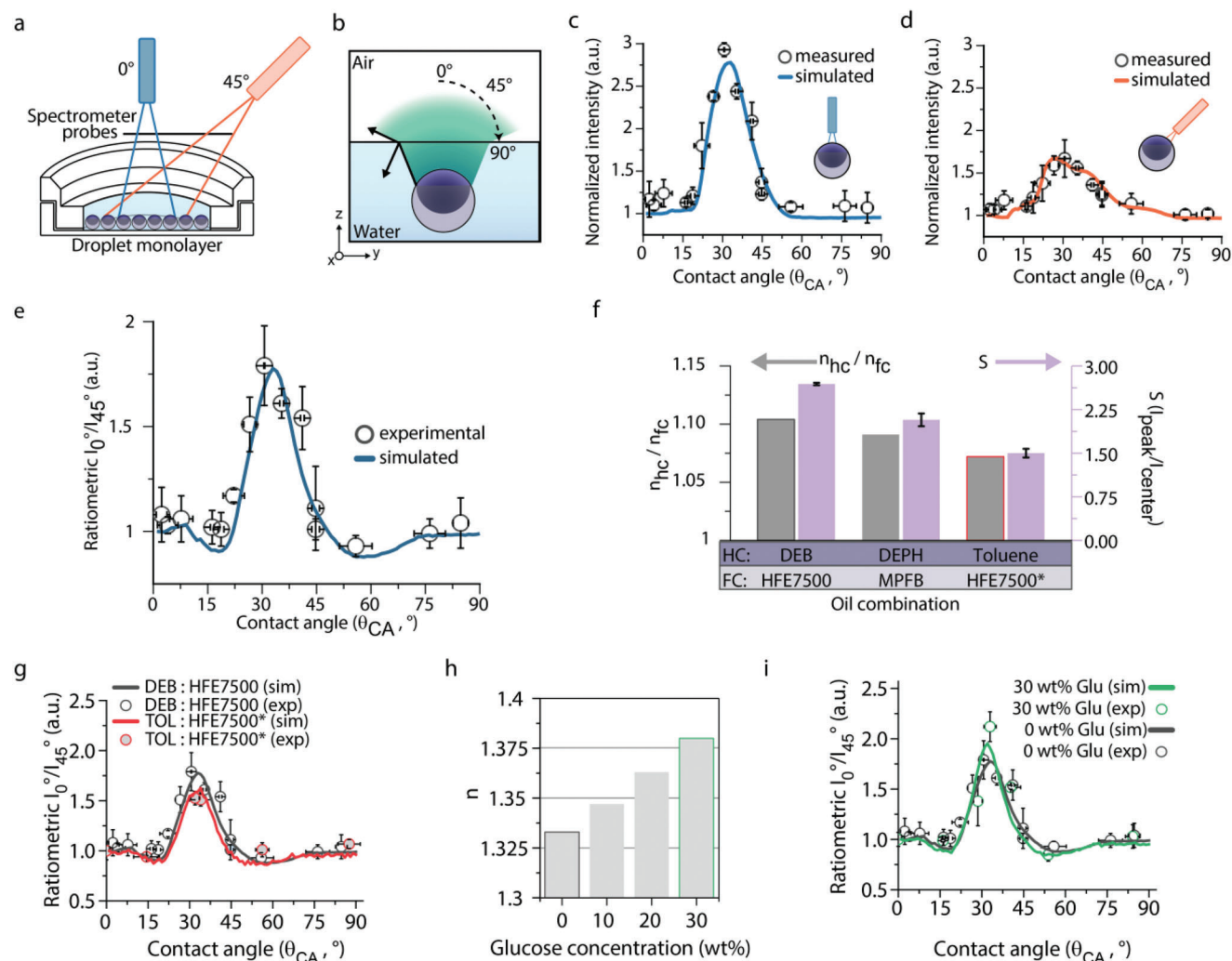


**Figure 5.** Experimental and simulated ratiometric emission intensity of fluorescent droplet layers. a) Schematic showing the two-probe detection setup, with one probe collecting light emitted in the vertical direction ( $0^\circ$ ) and one probe at an angle of  $45^\circ$ ; incident light  $\lambda = 385$  nm, emission intensity recorded at  $\lambda = 472$  nm. b) Schematic depicting the effect of the water–air interface on droplet emission and notation for emission direction. c) Modeled L-curve observed at  $0^\circ$  (blue trace) and measured emission intensities of DEB/HFE droplets in water (white circles) for emission between  $-12^\circ$  and  $12^\circ$  above the droplet. d) Modeled L-curve observed at  $45^\circ$  (red trace) and measured emission intensities of DEB/HFE droplets in water for emission between  $40^\circ$  and  $50^\circ$ . e) Ratiometric  $I_{0^\circ}/I_{45^\circ}$  curves predicted based on modeling results (blue trace) and the measured data obtained from perylene-loaded DEB/HFE polydisperse emulsion droplets located in the hydrocarbon phase. f) Refractive index contrast ( $n_{HC}/n_{FC}$ ) for three different reconfigurable complex emulsion droplet combinations featuring DEB:HFE7500 ( $n_{DEB,mix} = 1.47$ ,  $n_{HFE7500,mix} = 1.33$ ), diethyl phthalate (DEPH):methoxyperfluorobutane (MPFB) ( $n_{DEPH,mix} = 1.45$ ,  $n_{MPFB,mix} = 1.33$ ), and toluene:HFE7500 ( $n_{TOL,mix} = 1.45$ ,  $n_{HFE7500*,mix} = 1.35$ , \*FC phase is 9:1 HFE7500:FC43) with signal-to-noise ratio from line-profile intensities of droplets with  $\theta_{CA} \approx 30^\circ$ . g) Ratiometric  $I_{0^\circ}/I_{45^\circ}$  curves predicted based on simulated results (sim, line) and experimental data (exp, symbols) obtained from perylene-loaded DEB:HFE7500 and toluene:HFE7500\* droplets. h) Refractive index of continuous phases tuned with the addition of glucose at various concentrations (wt%). i) Simulated (sim, line)  $0/45^\circ$  ratiometric L-curve for DEB:HFE7500 droplets in different concentrations of glucose (0, 30 wt%) compared to measured ratiometric results in matching experimental conditions (exp, symbols).

placed polydisperse fluorescent Janus emulsion droplets as a thin layer into a sample holder and used a bifurcated fiber aligned in the vertical direction for both excitation light delivery and emitted light intensity collection. In addition, we positioned a second spectrometer probe oriented toward the sample at a  $45^\circ$  angle (Figure 5a). By simultaneously recording the light emitted from the polydisperse droplet assembly at  $0^\circ$  and  $45^\circ$  angles, we accurately detect small variations in droplet morphology and thus the three-phase contact angle in situ, alleviating the need for a more complicated microscopic imaging setup.

To account for the changed experimental setup within our model, we added the additional water–air interface to the simulation. The light delivery was adjusted to match the experimental conditions of the fiber optic setup (NA = 0.22), and the amplitude and direction of emitted light rays were recorded after exiting the water–air interface (Figure 5b). The additional water–air interface caused deviations from the theoretical radial emission profiles presented above (Figure 3e). While the direction and amplitude of vertically emitted rays remains largely unaffected, off-axis emitted rays undergo



refraction, and their amplitude reduces due to partial reflection.

To model the light collection for the two optical fiber probes positioned above a monolayer of droplets (at 0° and 45°) as a function of droplet morphology (Figure 5a), the angular emission intensities emanating from the droplets were summed within the probes' respective collection cones of ≈25° apex angle (Figure 5c,d). Then, a ratiometric light curve (L-curve) was generated by dividing the 0° emission intensity by the 45° emission intensity (Figure 5e).

We experimentally recorded and verified the modeled emission profiles using monolayers of monodisperse droplets and thin layers of polydisperse droplets. The morphology of the fluorescent droplets can be tuned by varying the ratio of the two surfactants, SDS and Zonyl, which enables continuous recording of the L-curves observed by the optical probes oriented at 0° and 45°. The graphs in Figure 5c–e reveal a close agreement between the theoretical predictions of the light intensities and the experimentally observed values for both optical probes. Droplets with a contact angle of  $\theta_{CA} \sim 30^\circ$  show a strong vertical emission signature, detected by the 0° probe, distinguishing this particular droplet configuration from other morphologies that are characterized by lower light emissions in the vertical direction. An increase of the three-phase contact angle to  $\theta_{CA} > 40^\circ$  increases the collected light intensity for the optical probe oriented at 45° to the sample. While the measured vertical emission peak is higher than the ratiometric peak, the ratiometric peak is self-referential, applicable to polydisperse emulsion samples, negating the effects of unequal dye loading, spatial distribution of droplets, and size-dispersivity volume effects of dye in view of the spectrometer probes.

The refractive index contrast defines the critical angle at which total internal reflection can occur. We probed different combinations of hydrocarbon and fluorocarbon oils that are compatible with the thermal phase separation approach for the generation of reconfigurable complex emulsion droplets (Figure 5f). The model combination in this study, DEB:HFE7500 ( $n_{DEB,mix} = 1.47$ ,  $n_{HFE,mix} = 1.332$ ), displayed the highest refractive index contrast (1.104) of tested systems. We tested two other combinations, namely, toluene:HFE7500:FC43 (9:1) ( $n_{TOL,mix} = 1.45$ ,  $n_{HFE*,mix} = 1.352$ ) and diethyl phthalate:methoxyperfluorobutane ( $n_{DEP,mix} = 1.452$ ,  $n_{MPFB,mix} = 1.331$ ), which displayed a smaller refractive index contrast of 1.072 and 1.091, respectively. In these combinations, due to the partial miscibility of hydrocarbon and fluorocarbon oils close to their respective upper critical solution temperature, the actual refractive index contrast differed from the literature values of the pure solvents (Figure 5a and Supporting Information Table S1).

Due to the subdued probability of total internal reflection as a result of the lowered refractive index contrast (Figure 5f), the light intensity within the hydrocarbon phase is reduced (Supporting Information Figure S7). These both affect incident light and emissive light total internal reflection at the hydrocarbon–fluorocarbon interface. For incident light, the increasing critical angle at the hydrocarbon–fluorocarbon interface increases the morphologies at which light can be totally internally reflected, widening the peak of total internally reflected incident light (Supporting Information Figure S7), enhancing fluorescence at the hydrocarbon–fluorocarbon interface and the signal-to-noise ratio

( $S = I_{peak}/I_{center}$ ) of emulsion droplets (Figure 5f). This affects the ratiometric (0°/45°) L-curve by reducing the signal-to-noise ratio of fluorescent emission from complex emulsion droplets, but does not affect the morphological contribution to angular droplet emission (Figure 5g).

By preparing droplets in solutions of glucose at various concentrations (0, 30 wt%), the refractive index of the aqueous continuous phase could be altered from  $n = 1.333$  for pure water to  $n = 1.380$  for 30 wt% glucose (Figure 5h). The addition of surfactant (up to 1 wt%) affected the refractive index by  $\Delta n < 0.001$  (Supporting Information Table S1). We used these measured values to simulate the behavior of collected and emitted light for droplets composed of DEB:HFE7500 at various morphologies (Figure 5h,i). For incident light to the droplets, by lowering the refractive index contrast between the aqueous continuous phase and the hydrocarbon phase, the lensing effect of the droplets was reduced, which enabled a larger fraction of incident light to be collected along the internal droplet interface (Supporting Information Figure S7). This effectively caused an enhancement of the influence of collected light on the final emission profile of the complex emulsion droplets (Figure 5i), where a larger peak intensity was found for the 0° L-curve, along with the width of the L-curve peak being reduced; and light collection of incident light was favored over the collection of emitted light purely along the internal interface (Figure 5i and Supporting Information Figure S7). These results demonstrate that Janus emulsions are experimentally robust for sensing applications, where the addition of high sugar concentrations or otherwise changing refractive indices of aqueous environment has a relatively minor optical contribution.

Building on our findings of enhanced signal-to-noise ratios due to a preferred excitation of emitters close to the internal interface of the droplets, we next hypothesized that this effect could be further amplified through the addition of a second emitter. In these experiments, we added a complimentary dye (*N,N'*-bis(2,6-diisopropylphenyl)-3,4,9,10-perylenetetracarboxylic diimide (PDI-O)) to the higher refractive index phase that presents an overlapping absorption and emission band with the perylene dyes (Figure 6a,b). As revealed in our ray-tracing model described above, the initial location of the emitters and their distance to the internal droplet interface affect the probability of total internal reflection within the DLCs. Thus, as a result of the significantly enhanced perylene emission intensity adjacent to the internal droplet interface, energy transfer from the blue perylene dye to the red PDI-O dye resulted in a preferred excitation of the latter in these regions of the droplet. When applying UV light ( $\lambda = 385$  nm) to droplets containing both dyes, the emitted light from high band gap perylene can be partially attenuated due to the spectral overlap with the low band gap PDI-O dye. The increased excitation probability of PDI-O within the region of interest for TIR resulted in a significant enhancement of the localized emission adjacent to the three-phase contact line when compared to solely perylene-containing droplets, as revealed by the line profiles from the respective fluorescence micrographs of the droplets (Figure 6c). To compare the enhanced signal-to-noise ratio of the red PDI-O emission at the expense of totally internally reflected blue perylene emission in macroscale experiments, we monitored the vertical emission intensity of droplet monolayers in the blue region corresponding to perylene emission

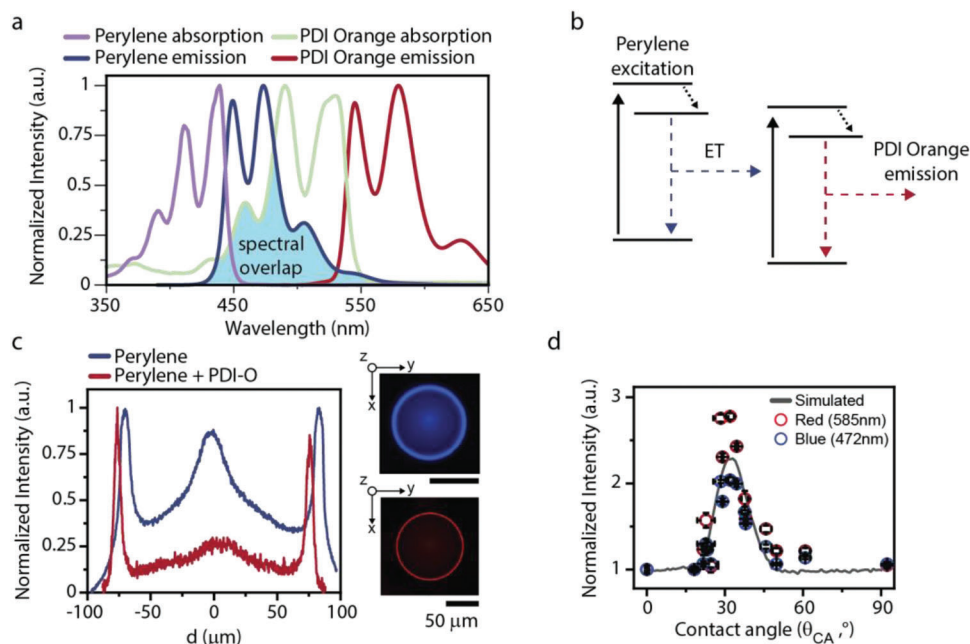


**Figure 6.** Enhancement of signal-to-noise ratio via compartmentalization of two emitters with an overlapping absorption and emission band. a) Measured absorption and emission spectra for perylene and PDI-O. b) Schematic diagram showing the attenuation of the perylene emission through absorption by the PDI-O dye. c) Line-profile intensities for droplets containing only perylene dye versus droplets containing perylene and PDI-O in the hydrocarbon phase, with corresponding fluorescence micrographs (incident light wavelength = 385 nm, light delivery from below, scale bar = 50  $\mu\text{m}$ , normalized between 0 and 1). d) Vertical emission intensity of droplets in varying morphologies containing perylene and PDI-O, resulting in an L-curve for the blue region (472 nm, corresponding to perylene emission) and red region (585 nm, corresponding to PDI-O), compared to the emission L-curve derived from simulations.

( $\lambda = 472$  nm) and the red region corresponding to PDI-O emission ( $\lambda = 585$  nm). A comparison of the resulting L-curves to simulations of the expected morphology-dependent droplet emission intensities showed that the peak emission intensity of perylene (472 nm) was decreased with respect to the simulations, whereas the PDI-O emission showed a significantly (2.78-fold) increased peak intensity (Figure 6d), thus confirming an enhancement of the luminescence concentration via the sequential absorption-emission cascade.

### 3. Conclusion

Bi-phasic fluorescent Janus emulsion droplets exhibit dynamically tunable angle-dependent light-emission profiles that significantly depend on the droplet composition and internal geometry. Janus emulsion droplets comprised of a hydrocarbon and fluorocarbon oil with the fluorescent dye perylene incorporated in the hydrocarbon phase display a range of morphologies that can sustain total internal reflection and light concentration near the droplets' internal interface. In these droplet morphologies, incident light is directed along the internal interface via total internal reflection leading to much higher light concentration near the internal interface as compared to the bulk of the hydrocarbon phase. Consequently, more of the fluorescent dye is excited near the internal interface generating a pronounced fluorescence. The emitted light is then again guided along the internal interface by total internal reflection and ultimately escapes the droplets near the three-phase contact line at a morphology-dependent angle creating a distinct angle-dependent emission profile. We

established a custom-designed theoretical ray-tracing algorithm that models, with predictive capability, the angle-dependent light-emission intensity of bi-phasic Janus emulsions with different chemical composition and refractive index contrasts. Angle-dependent fluorescence micrographs of droplets with different internal interface curvature and three-phase contact angle closely corroborate the ray-tracing predictions. To demonstrate the utility of fluorescent bi-phase emulsion droplets for dynamic chemical sensing applications, we established a ratiometric optical read-out strategy for chemically triggered in situ variations in droplet morphology, based on capturing light emitted by the droplets in two distinctly different angle ranges and present ratiometric intensity calibration curves for droplets in different morphologies that take into account actual experimental conditions and very closely match our model predictions. The ratiometric identification of droplet morphologies provides the sensitivity to detect small changes in droplet morphology using either a single or alternatively two emissive dyes inside the higher refractive index fluid and is robust and insensitive to polydispersity of the microscale optical elements. Furthermore, the ratiometric light curve (L-curve), combined with ray-tracing modeling, enabled the investigation and optimization of experimental conditions in emulsion composition. Together, our findings provide a solid foundation for understanding the angle-dependent light-emission output of fluorescent bi-phase emulsion droplets and facilitate in situ monitoring of small changes in droplet morphology that result from chemical or physical stimuli in the droplet's vicinity. The sensitivity of the fluorescent droplet morphology to subtle changes in their chemical and physical environment

paired with a macroscopically measurable fluorescent signature that is strongly dependent on the droplet morphology makes these easily tailored emulsion systems a promising material platform for chemical, physical, and biological sensing scenarios that require high sensitivity, fast turn-around, or high spatial resolution at low cost. Dynamic fluid material platforms capable of altering fluorescence signals in response to chemical and physical stimuli may further play an important role and offer enticing opportunities for the development of dynamic microoptical components, including for applications in displays and the generation of optical metamaterials.

## Supporting Information

Supporting Information is available from the Wiley Online Library or from the author.

## Acknowledgements

Open access funding enabled and organized by Projekt DEAL. The authors gratefully acknowledge funding through the Emmy Noether program of the German Research Foundation (DFG) under grant no. ZE1121/3-1. S. N. and M. K. acknowledge support by the US Army Research Office through the Institute for Soldier Nanotechnologies at MIT under contract no. W911N-F1-3-D001.

Open access funding enabled and organized by Projekt DEAL.

## Conflict of Interest

The authors declare no conflict of interest.

## Data Availability Statement

The data that support the findings of this study are available in the supplementary material of this article.

## Keywords

complex colloids, fluorescent probes, Janus particles, microfluidics, microlenses, total internal reflection

Received: April 13, 2023

Revised: June 7, 2023

Published online: July 23, 2023

- [1] A. A. Nagarkar, S. E. Root, M. J. Fink, A. S. Ten, B. J. Cafferty, D. S. Richardson, M. Mrksich, G. M. Whitesides, *ACS Cent. Sci.* **2021**, *7*, 1728.
- [2] V. Montes-García, M. A. Squillaci, M. Diez-Castellnou, Q. K. Ong, F. Stellacci, P. Samorì, *Chem. Soc. Rev.* **2021**, *50*, 1269.
- [3] T. M. Swager, *Angew. Chem., Int. Ed.* **2018**, *57*, 4248.
- [4] C. A. Bertrand, *Science* **2001**, *293*, 1335.
- [5] L. Zeininger, S. Nagelberg, K. S. Harvey, S. Savagatrup, M. B. Herbert, K. Yoshinaga, J. A. Capobianco, M. Kolle, T. M. Swager, *ACS Cent. Sci.* **2019**, *5*, 789.
- [6] T. M. Choi, K. Je, J.-G. Park, G. H. Lee, S.-H. Kim, *Adv. Mater.* **2018**, *30*, 1803387.
- [7] L. Shui, R. A. Hayes, M. Jin, X. Zhang, P. Bai, A. Van Den Berg, G. Zhou, *Lab Chip* **2014**, *14*, 2374.
- [8] A. Bigdeli, F. Ghasemi, H. Golmohammadi, S. Abbasi-Moayed, M. A. F. Nejad, N. Fahimi-Kashani, S. Jafarinejad, M. Shahrabadian, M. R. Hormozi-Nezhad, *Nanoscale* **2017**, *9*, 16546.
- [9] Q. He, H. Vijayamohan, J. Li, T. M. Swager, *J. Am. Chem. Soc.* **2022**, *144*, 5661.
- [10] D. H. Ho, Y. Y. Choi, S. B. Jo, J.-M. Myoung, J. H. Cho, *Adv. Mater.* **2021**, *33*, 2005846.
- [11] D. Vanmaekelbergh, L. K. Van Vugt, H. E. Bakker, F. T. Rabouw, B. De Nijs, R. J. A. Van Dijk-Moes, M. A. Van Huis, P. J. Baesjou, A. Van Blaaderen, *ACS Nano* **2015**, *9*, 3942.
- [12] J. Reichstein, S. Schötz, M. Macht, S. Maisel, N. Stockinger, C. C. Collados, K. Schubert, D. Blaumeiser, S. Wintzheimer, A. Görling, M. Thommes, D. Zahn, J. Libuda, T. Bauer, K. Mandel, *Adv. Funct. Mater.* **2022**, *32*, 2112379.
- [13] G. Kamita, B. Frka-Petesic, A. Allard, M. Dargaud, K. King, A. G. Dumanli, S. Vignolini, *Adv. Opt. Mater.* **2016**, *4*, 1950.
- [14] A. E. Goodling, S. Nagelberg, B. Kaehr, C. H. Meredith, S. I. Cheon, A. P. Saunders, M. Kolle, L. D. Zarzar, *Nature* **2019**, *566*, 523.
- [15] J. Heikenfeld, K. Zhou, E. Kreit, B. Raj, S. Yang, B. Sun, A. Milarcik, L. Clapp, R. Schwartz, *Nat. Photonics* **2009**, *3*, 292.
- [16] T. Leydecker, M. Herder, E. Pavlica, G. Bratina, S. Hecht, E. Orgiu, P. Samorì, *Nat. Nanotechnol.* **2016**, *11*, 769.
- [17] J. Reichstein, S. Müssig, H. Bauer, S. Wintzheimer, K. Mandel, *Adv. Mater.* **2022**, *34*, 2202683.
- [18] G. Paris, J. Heidepriem, A. Tsouka, Y. Liu, D. S. Mattes, S. Pinzón Martín, P. Dallabernardina, M. Mende, C. Lindner, R. Wawrzinek, C. Rademacher, P. H. Seeberger, F. Breitling, F. R. Bischoff, T. Wolf, F. F. Loeffler, *Adv. Mater.* **2022**, *34*, 2200359.
- [19] L. You, D. Zha, E. V. Anslin, *Chem. Rev.* **2015**, *115*, 7840.
- [20] J. R. Askim, M. Mahmoudi, K. S. Suslick, *Chem. Soc. Rev.* **2013**, *42*, 8649.
- [21] S. Savagatrup, D. Ma, H. Zhong, K. S. Harvey, L. C. Kimerling, A. M. Agarwal, T. M. Swager, *ACS Sens.* **2020**, *5*, 1996.
- [22] B. McKenna, R. C. Evans, *Adv. Mater.* **2017**, *29*, 1606491.
- [23] P. Simón Marqués, B. D. Frank, A. Savateev, L. Zeininger, *Adv. Opt. Mater.* **2021**, *9*, 2101139.
- [24] J.-H. Kim, J.-H. Kim, *ACS Photonics* **2015**, *2*, 633.
- [25] P. S. Marqués, M. Krajewska, B. D. Frank, K. Prochaska, L. Zeininger, *Chem. - Eur. J.* **2023**, *29*, e202203790.
- [26] C.-J. Lin, L. Zeininger, S. Savagatrup, T. M. Swager, *J. Am. Chem. Soc.* **2019**, *141*, 3802.
- [27] J. Li, A. Concellón, K. Yoshinaga, Z. Nelson, Q. He, T. M. Swager, *ACS Cent. Sci.* **2021**, *7*, 1166.
- [28] Q. Zhang, L. Zeininger, K.-J. Sung, E. A. Miller, K. Yoshinaga, H. D. Sikes, T. M. Swager, *ACS Sens.* **2019**, *4*, 180.
- [29] S. Müssig, J. Reichstein, F. Miller, K. Mandel, *Small* **2022**, *18*, 2107511.
- [30] R. V. Balaj, L. D. Zarzar, *Chem. Phys. Rev.* **2020**, *1*, 011301.
- [31] S. Nagelberg, L. D. Zarzar, N. Nicolas, K. Subramanian, J. A. Kalow, V. Sresht, D. Blankschtein, G. Barbastathis, M. Kreysing, T. M. Swager, M. Kolle, *Nat. Commun.* **2017**, *8*, 14673.
- [32] Y. Yang, J. B. Kim, S. K. Nam, M. Zhang, J. Xu, J. Zhu, S.-H. Kim, *Nat. Commun.* **2023**, *14*, 793.
- [33] A. Saunders, L. Zarzar, *Proc. SPIE* **2020**, *11292*, 112920X.
- [34] L. Zeininger, E. Weyandt, S. Savagatrup, K. S. Harvey, Q. Zhang, Y. Zhao, T. M. Swager, *Lab Chip* **2019**, *19*, 1327.
- [35] L. D. Zarzar, V. Sresht, E. M. Sletten, J. A. Kalow, D. Blankschtein, T. M. Swager, *Nature* **2015**, *518*, 520.
- [36] S. Djalali, B. D. Frank, L. Zeininger, *Soft Matter* **2020**, *16*, 10419.
- [37] B. D. Frank, M. Antonietti, L. Zeininger, *Macromolecules* **2021**, *54*, 981.
- [38] Y. Guo, Y. Fang, K. Jia, Y. Yu, L. Yu, H. Li, J. Zhang, X. Zheng, L. Huang, W. U. Wen, Y. Mai, *Macromol. Rapid Commun.* **2021**, *42*, 2100085.

- [39] B. D. Frank, M. Perovic, S. Djalali, M. Antonietti, M. Oschatz, L. Zeininger, *ACS Appl. Mater. Interfaces* **2021**, *13*, 32510.
- [40] D. Fong, T. M. Swager, *J. Am. Chem. Soc.* **2021**, *143*, 4397.
- [41] V. Trinh, C. S. Malloy, T. J. Durkin, A. Gadh, S. Savagatrup, *ACS Sens.* **2022**, *7*, 1514.
- [42] M. Pavlovic, H. K. Ramiya Ramesh Babu, S. Djalali, M. Vraneš, V. Radonić, L. Zeininger, *Anal. Chem.* **2021**, *93*, 9390.
- [43] M. Pavlovic, H. K. Ramiya Ramesh Babu, S. Djalali, Z. Pavlovic, M. Vraneš, L. Zeininger, *Langmuir* **2023**, *39*, 2152.
- [44] S. Djalali, P. Simón Marqués, B. D. Frank, L. Zeininger, *Adv. Funct. Mater.* **2022**, *32*, 2107688.
- [45] J. Li, S. Savagatrup, Z. Nelson, K. Yoshinaga, T. M. Swager, *Proc. Natl. Acad. Sci. USA* **2020**, *117*, 11923.
- [46] B. D. Frank, S. Djalali, A. W. Baryzewska, P. Giusto, P. H. Seeberger, L. Zeininger, *Nat. Commun.* **2022**, *13*, 2562.
- [47] B. Barua, T. J. Durkin, I. M. Beeley, A. Gadh, S. Savagatrup, *Soft Matter* **2023**, *19*, 1930.